An Image Based Approach to Recovering the Gravitational Field of Asteroids

Andrew Melim
Andrew.Melim@gatech.edu
Frank Dellaert
dellaert@cc.gatech.edu

College of Computing
Georgia Institute of Technology
Atlanta GA, 30332 USA

Abstract

NASA's DAWN spacecraft is on a mission to recover the gravity and structure of the asteroids Vesta and Ceres. Current approaches for developing a gravitational map of a celestial body rely upon use of the Deep Space Network of radio telescopes in conjunction with camera measurements for highly accurate tracking of orbiting bodies. Unfortunately, large occluding bodies greatly effect the accuracy of the radio tracking system, significantly reducing the time available for scientific experiments. This paper presents a Structure from Motion based approach that recovers the gravitational map as well as the asteroid's structure in a two step optimization process. The approach solves for a set of spherical harmonic coefficients that define the gravitational potential given a spacecrafts relative position to the asteroid without the need for radiometric tracking from Earth based satellites. The resulting procedure can then be used to augment gravitational science during periods of large noise or damaged equipment. Results are shown using the Vesta dataset from the DAWN mission and are compared with the recently published results from the DAWN gravitational team.

1 Introduction

This paper presents a pure vision based approach to solving for the gravitational field of extraterrestrial bodies with image data obtained by an orbiting spacecraft or satellite. Recovering a spacecraft's trajectory with modern day Structure from Motion approaches allows for further investigation for perturbations to accelerations due to variation in the strength of gravity. Understanding the variations of these forces, as well as developing a map, help to derive various models on the interior structure of the target planetary body or asteroid[1, 11].

Classical approaches for recovering the strength of a gravitational field study the motion of a satellite by tracking its position with Earth based telescopes [8, 19]. The basic principle behind this approach was developed in the field of satellite geodesy with the specific goal to define a highly accurate map of Earth's gravitational field. The same principle has not changed significantly, where the use of X-band Doppler and range measurements from a collection of Earth based tracking stations, known as the Deep Space Network (DSN), has been used to great effect. Results from the Mars Reconnaissance Orbiter (MRO) used DSN tracking exclusively to determine high resolution models of gravity field including seasonal gravity changes, gravitational mass, and tidal information [12].

Computer vision approaches have also been used to assist Earth based tracking systems in certain situations. NASA's NEAR-Shoemaker mission developed detailed 3D reconstructions and gravity estimation of the near Earth asteroid Eros [11, 17]. DSN tracking was augmented with visual landmark data collected from an on-board camera. Each landmark observation provides angle measurements in two directions of the spacecraft position relative to the Eros surface. Landmarks were determined from craters that widely varied in size on the surface of Eros. The position is defined as the crater center projected onto the plane tangent to the crater rim. Craters were classified by size and measured over a series of varied radius orbits around Eros. While effective, this approach required specific maneuvers from the spacecraft to properly determine the landmarks.

More recent missions have utilized algorithms similar to photometric stereo to augment DSN tracking data [5, 16]. NASA's DAWN spacecraft was launched to perform detailed studies of the two largest asteroids in our solar system, Vesta and Ceres [10, 13] . DAWN's gravity estimation is assisted with the use of small maplets, known as L-Maps, that describe local areas centered on a landmark control point [5, 6]. Construction of L-maps consists of approximating a brightness model for each pixel within an area centered on a chosen control point over at least three images. Albedo and slope information is then optimized using least square fit between the measured brightness and the provided brightness model. Height information is then calculated through a relaxation process. Estimation of the spacecraft state is limited only to position and a semi-kinematic solution. After optimization, landmark positions are then used with a navigation filter with radiometric measurements to improve spacecraft state estimation. However, the construction of each maplet requires apriori information on the camera location, obtained from tracking data, and multiple exposures with varying illumination in order to obtain accurate maplets. More crucially, these approaches still rely on the use of tracking data in order to properly assemble maplets into a global 3D reconstruction and gravity solution [13].

Although these approaches are very accurate and reliable, they are also extremely reliant upon constant, uninterrupted, radiometric tracking measurements from Earth-based stations. Many of them utilize optical data to augment their solution, yet none present a complete pipeline that can be used in the case of equipment failure, long distance tracking noise, or during the large periods of time when the sun and other large bodies corrupt the radio tracking data. A pure vision based approach is required to obtain gravitational estimates for future missions looking to explore planets, asteroids, and other extraterrestrial bodies in the outer solar system. DSN tracking can only support a single mission at the time, limiting the number of spacecraft that can be launched and supported by the network. Additionally, tracking stations are beginning to degrade and suffer from lapses in support and funding due to recent economic situations.

This paper introduces a method to recover an estimate of the gravitational field without any need of radiometric tracking. We formulate constraints on a set of spherical harmonic coefficients, which defines a map of gravitational variations on a sphere, that integrate with graphical models used in modern Structure from Motion techniques. Our approach is a complete image-based pipeline based around a two-step optimization that recovers 3D structure, spacecraft kinematics, and a gravitational model. We present our results in recovering the gravitational potential of the asteroid Vesta utilizing data from the DAWN mission up to degree three for the spherical harmonic coefficients, comparing to the result from the DAWN gravitational team [13].

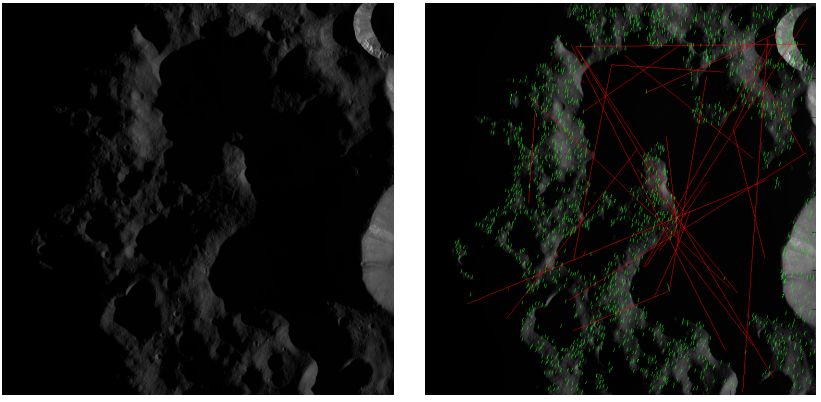

(a) (b)

Figure 1: Example images a High Alititude Orbit from the DAWN spacecraft dataset around Vesta. **(a)** Source image of partially illuminated craters. **(b)** Feature matching results with a successive image. Green tracks show inlier matches with red tracks indicating outlier matches.

2 Optimization Technique

The basic process for gravity estimation is a two step iterative optimization. First, spacecraft pose and 3D landmark variables are estimated using batch bundle adjustment. The second step involves optimizing for the parameters of the gravitational field, in addition to camera pose velocities, using the local solutions found in step one. Here, tracking residuals are minimized with respect to global models. The residual errors for the global model are defined through kinematic error as well as a power law constraint.

We formulate the problem using a factor graph $G = (F, \Theta, E)$ containing a set of factor nodes $f_\alpha \in F$, variable nodes $\theta_\beta \in \Theta$, and edges $e_{\alpha\beta} \in E$ connecting factors to variables if and only if the variable θ_β is involved with factor f_α.

Finding the maximum a posteriori density to the factorization $f(\Theta)$ of the graph corresponds to finding the assignment of all variables $\hat{\theta}$ that minimizes the negative log-likelihood

$$\hat{\Theta} = argmim\left(-log(f(\Theta))\right) \tag{1}$$

2.1 Bundle Adjustment Optimization

Camera measurements from $x_j \in J$ views observing $l_k \in K$ 3D landmark points are optimized in a batch monocular bundle adjustment step. Similar to many recent feature-based SLAM approaches [3, 9, 14], the optimization exploits the sparsity structure of the problem between the landmarks and camera poses. Camera pose initialization is computed using relative pose computations after running RANSAC loop using a fundamental matrix kernel [2, 7]. Features are found using the SIFT detector and descriptor [15].

The camera unknowns are inserted into a factor graph with a binary error constraint minimizing the re-projection error with an image measurement $z_v \in \mathbb{R}^2$

$$e_{proj} = ||p(x_j, l_k) - z_v||^2_\Sigma \tag{2}$$

Due to the specific texture and surface of the asteroid, we found that there was a fairly high percentage of outliers when performing the initial descriptor matching. In order to

improve the quality of the initial estimate, an additional verification step is performed to weed out any possible outliers that survived the initial geometric verification step.

Given three overlapping images, I_1, I_2, I_3, we define any feature which is matched between image pairs (I_1, I_2) , (I_2, I_3), and (I_1, I_3) as a triplet. In order to avoid $O(n^2)$ matching to verify, we make use of a disjoint set forest data (DSF) structure[4] to efficiently partitions sets of cameras based on shared feature matches. The DSF consists of two simple functions, an **insertion** of an element with a key, and a **union** that recursively merges any elements with a shared key. The union operation on the set joints any two elements sharing the same key into a single element in $O(log\, n)$ time, a vast improvement on the polynomial time it would take to perform a simple comparison between all feature matches.

Over the set of all feature matches for the cameras J, a visibility graph is constructed with edges e_j connecting camera poses if there exist a set of inlier matches from the RANSAC loop greater than a threshold e_{thresh}. We found, experimentally, that a value of $e_{thresh} = 20$ was sufficient for the Vesta dataset. Triplet verification iterates all possible combinations of two match edges $e_j, e_{j+i}$and inserts their camera poses as a single element into the disjoint set forest, using the feature index as a key. Union of these camera poses and corresponding keys will partition them into sets of cameras that all view the same feature. Determination of a feature triplet then simply requires the verification of any partition's size is of dimension three. Once features have been verified, they are initialized using a direct linear transformation (DLT) based triangulation and a corresponding projection factor is inserted into the factor graph for optimization.

2.2 Gravitational Model Optimization

The second step of the optimization aims to minimize the error of a dynamically integrated trajectory given an initial position $x_j \in \mathbb{R}^3$ with an expected final position x_{j+t} computed from the SfM solution. Assuming that no other forces are effecting the path of the spacecraft, the error directly corresponds to solving for the initial velocity for the trajectory as well as the strength of the accelerations that alter the velocity of the spacecraft.

Recovering the gravity requires uninterrupted tracks of spacecraft motion, specifically ensuring that no thruster maneuvers occur between camera measurements. Our approach does explicitly solve for any forces that effect motion apart from gravity, ignoring solar radiation pressure on the spacecraft's solar panels and n-body gravity forces from other bodies such as the sun and nearby planets.

Define a track T to be a stretch of uninterrupted motion of the spacecraft, discretized by a set of camera poses $x_j \in X(T)$. We further split each track into a set of small tracklets of length t where the end of each track is computed from

$$x_{j+t} = h(x_j, v_j, t) \tag{3}$$

The function $h(x_j, v_j, t)$ is the numerical integration of the spacecraft's dynamics using Cowell's formula Eq. 9 over time t. Integration is performed with single-step Euler integration.

Velocity of the initial pose for each tracklet v_j is not immediately recovered from the first-stage optimization. An approximation of the velocity can be computed using visual odometry between each camera measurement, however when camera measurements are sparse and only periodically captured, this approach can be fairly inaccurate. Instead, optimization of the initial velocity in conjunction with the gravitational field is required to obtain more accurate results. Our approach computes initial estimates for velocity from the pose solution found from the first-stage optimization solution with a finite difference method.

3 Gravitational Fields

We develop the construction of our two gravitational constraints with the classical representation of gravitational fields using spherical harmonic coefficients [8, 19].

The force of gravity $F_g \in \mathbb{R}^3$ of an asteroid acting on a spacecraft is described by the 2-Body equation:

$$F_g = \frac{Gm_a m_{sc}}{r^3} x \tag{4}$$

with the spacecraft's position $x \in \mathbb{R}^3$ relative to the asteroid's fixed inertial frame, masses $m_a, m_{sc} \in \mathbb{R}$ of the asteroid and spacecraft respectively, the distance between the two bodies r, and the gravitational constant of the asteroid $G \in \mathbb{R}$. Since the difference between the mass of an asteroid and spacecraft is significantly larger by several orders of magnitude, we can simplify by replacing Gm_a with a constant μ, to obtain the relative form of Eq. 4

$$F_g = \frac{\mu}{r^3} x \tag{5}$$

Taking the gradient of the potential $V = \frac{\mu}{r}$ provides an acceleration vector $\ddot{x} = \nabla V$ between the two centers of mass. However, the acceleration from the potential in Eq. 5 assumes that the mass of the asteroid is completely uniform, as well as ignores other external forces such as those due to control actuation on the spacecraft, solar radiation pressure, and other nearby celestial bodies.

We are more interested in computing **perturbations** on the acceleration computed in Eq. 5 from non-central forces, specifically those due to the shape and irregular densities the asteroid. Obtaining an accurate model of the gravitational field beyond the two-body forces allows for improved orbit calculations, as well as provide insight into the mass distribution and mineral composite of the asteroid. One of the most useful components of the perturbation accelerations is in determining the oblateness of the body, a significant source of deviation from the 2-Body solution.

3.1 Gravitational Potential

The potential of the perturbations can be defined through the use of fully normalized associated Legendre polynomials $P_{n,m}$ and corresponding spherical harmonic coefficients $(C_{n,m}, S_{n,m})$; n, m are referred to as the degree and order of the coefficients, respectively. The spherical harmonics, commonly referred to as Stokes coefficients, define a basis for the gravitational model, similar to a Fourier series but instead map to the surface of a unit sphere.

The perturbation forces given the spacecraft's latitude, longitude, and altitude $(\phi_{sc}, \lambda_{sc}, r)$, referred to as the ephemeris, are described by an aspherical-potential function U [8]

$$U = \frac{\mu}{r} + \sum_{n=2}^{\infty} \sum_{m=0}^{l} P_{n,m}\left(sin(\phi_{sc})\right) \left\{C_{n,m} cos(m\lambda_{sc}) + S_{n,m} sin(m\lambda_{sc})\right\} \tag{6}$$

The potential function assumes that the degree one coefficients are zero since this defines the origin of the coordinate system at the center of mass, hence the summation begins with $n = 2$. When $m = 0$ coefficients are referred to as zonal, $n = m$ are sectoral coefficients, and $n! = m$ are tesseral. Zonal coefficients are commonly represented as $J_n = -C_{n,0}$ since $S_{n,0} = 0$. The coefficient J_2 is particularly interesting since it is mainly governed by the aforementioned oblateness of the body. One issue does arise from asteroids with strong

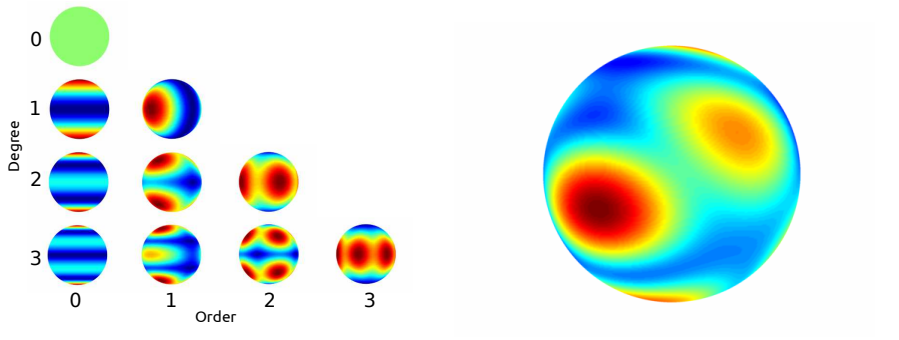

(a) (b)

Figure 2: **(a)** Gravitational field strength with harmonic coefficients of degree n and order m. **(b)** Vesta gravitational perturbations due to harmonics up to degree $n = 3$. The coefficient J_2 is commonly removed due to its dominating power over the other coefficients.

elliptical shapes, such as Eros and Vesta, where the spherical solution may not converge properly. For example, in the case of the Vesta solution, it was found that spherical harmonics were sufficient to obtain accurate result for interior modeling [13], the Eros result required the use of Ellipsoidal harmonic functions.

It's common to use normalized coefficients $(\bar{C}_{n,m}, \bar{S}_{n,m})$ in Eq. 6 since the typical order of magnitude for them can cause numerical issues during computation. Likewise, the Legendre polynomials must also be normalized during computation [19]. The normalization of the coefficients is performed by

$$\begin{bmatrix} \bar{C}_{n,m} \\ \bar{S}_{n,m} \end{bmatrix} = \sqrt{\frac{(n+m)!}{(n-m)!k(2n+1)}} \begin{bmatrix} C_{n,m} \\ S_{n,m} \end{bmatrix} \tag{7}$$
$$k = 1 \quad if \quad m = 0$$
$$k = 2 \quad if \quad m \neq 0$$

The accelerations acting on the spacecraft due to the perturbing potential $\ddot{x}_{pert} \in \mathbb{R}^3$ can be found by taking the gradient of Eq. 6

$$\ddot{x}_{pert} = \frac{\partial U}{\partial r}\left(\frac{\partial r}{\partial x}\right) + \frac{\partial U}{\partial \phi_{sc}}\left(\frac{\partial \phi_{sc}}{\partial x}\right) + \frac{\partial U}{\partial \lambda_{sc}}\left(\frac{\partial \lambda_{sc}}{\partial x}\right) \tag{8}$$

Effects of the perturbations on the total gravitational acceleration is expressed in Cowell's formula, which is readily plugged into a numerical integration method.

$$\ddot{x}_{total} = \frac{\mu}{r^3}x + \ddot{x}_{pert} \tag{9}$$

Determining the gravitational field now consists of finding a set of harmonic coefficients up to degree and order N

$$q = (c_{n,m}, s_{n,m})\ \forall n, m \leq N \tag{10}$$

and initial tracklet velocity v_j that agree with all measured tracklet poses x_{j+t} of an object in orbit around the asteroid, corresponding to the following least-squares term

$$e_{grav} = ||h(x_j, v_j, t, q) - x_{j+t}||^2_{\Sigma} \tag{11}$$

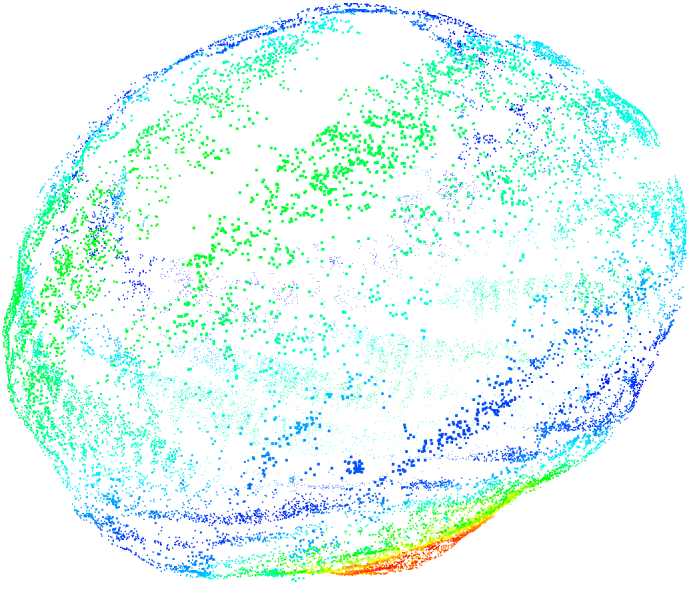

Figure 3: Vesta 3D Reconstruction (29143 landmarks) color mapped with our gravitational field results

An additional constraint is applied to the optimization in the form of the Kaula power law [8], which states that the RMS magnitude M_n of the coefficients of degree n tends to decay:

$$M_n = \sqrt{\frac{\sum_{m=0}^{l}(\bar{C}_{n,m}^2 + \bar{S}_{n,m}^2)}{(2n+1)}} \approx \frac{k_{vesta}}{n^2} \tag{12}$$

where $k_{vesta} = 0.011$.

A weighted error term is added to the optimization based on the coefficents deviation from the power law. Weights were chosen for each degree based upon hypothesized deviation from the power law as presented by Konopliv *et al.* [10]. Since higher degree coefficients follow the law more closely, the weights increase with the degree of the coefficient.

4 Results

We evaluated our approach using camera data from the DAWN spacecraft's orbits around 4 Vesta, the second largest asteroid in the Solar System. The dataset comprises of multiple different orbit maneuvers at varying altitudes. The survey orbit provided the main goal of surface spectral and mineral composition with the use of the Visual and Infrared Recorder (VIR). Primary gravity science measurements were taken during 50 days of high altitude mapping orbits (HAMO) at approximately 700-km altitudes, as well as a 200-km altitude low altitude mapping orbits (LAMO). Each of the two phases consists of X-band Doppler tracking in addition to optical data from an on-board camera. Camera calibration for geometric distortion in addition to sensor exposure settings, CCD bias and sensitivity is found from the detailed computation included with the dataset.

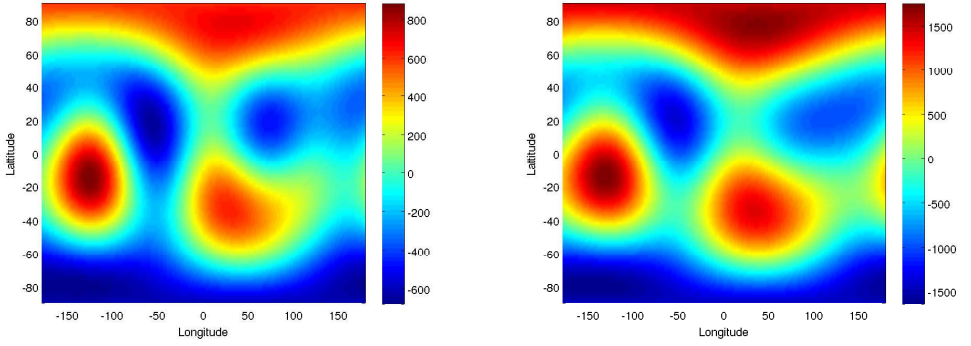

(a) (b)

Figure 4: Gravity perturbation field results **(a)** VESTA20H solution utilizing all HAMO + LAMO data with DSN tracking and optical landmarks **(b)** Our solution from a subset of HAMO-1 data using optical measurements only

Our results recover gravity from the first set of high altitude orbits (HAMO-1). Several maneuvers were required to adjust the spacecraft periodically during both the HAMO and LAMO phases. A set of orbits separated by a control maneuver are defined as a cycle. HAMO-1 contains eight cycles, each with different coverage patterns in order to image certain locations with higher accuracy. Cycles three and four provide the best coverage for the first HAMO cycle with 998 images. From this set of images, the tracks T used for gravity recovery consisted of approximately 50 images each, with a tracklet length t of three images.

Figure 3 shows our 3D reconstruction of Vesta color-mapped with the optimized gravitational perturbations recovered from our two-step optimization. The 3D reconstruction from cycles three and four estimated 29143 3D landmarks. The magnitude of the gravitational perturbations shown were taken from the L2-Norm of the accelerations computed in Eq. 8

Table 1 shows the comparative results from our approach against the VESTA20H solution recently published in Konopliv *et al.* [13]. The VESTA20H solution is computed from both sets of high altitude as well as the low altitude orbits using DSN tracking in addition to optical landmark tracking. VESTA20H solution computes the gravitational field up to degree twenty. The first three coefficients from VESTA20H are displayed along with our solution that was optimized up to a total of degree three, the maximum degree available from Konopliv *et al.* [13].

Figure 4 compares the two results Table 1 by looking at perturbation acceleration difference from the 2-body solution (mgals) given a spacecraft ephemeris (ϕ, λ, r) with reference radius $r = 256km$. Since the J_2 coefficient dominates the magnitude of the perturbation accelerations, it is removed from this visualization to compare the complexity of the higher order coefficients.

4.1 Analysis

As seen in Figure 4, the structure of the perturbation field is mostly recovered compared with the VESTA20H. The most significantly difference is found in the relative magnitudes between the two fields. The disparity between these two results can more readily be rectified by the fact that the ground truth data is a subset of the true solution computed up to degree

Coefficient	Konopliv13 VESTA20H (DSN + Optical)		Our Method (Optical Only)	
J_2	3.1779397e-2		10.8606e-2	
J_3	-3.3105530e-3		-7.94259e-3	
C_{21}, S_{21}	1.23e-9	-1.13e-9	-1.54692e-4	2.07609e-4
C_{22}, S_{22}	1.0139517e-3	4.2469730e-3	2.40848e-3	1.02151e-2
C_{31}, S_{31}	2.0456938e-3	1.6820966e-3	4.97394e-3	4.05602e-3
C_{32}, S_{32}	6.5144047e-4	-1.2177599e-3	6.51426e-4	1.21777e-3
C_{33}, S_{33}	2.3849359e-3	1.5466248e-4	2.38494e-3	1.07797e-4

Table 1: Coefficient solutions up to degree and order three. Solutions from Konopliv up to degree 3 are taken a full degree 20 solution, while our results are only computed to degree 3 in total.

twenty. The accelerations from higher coefficients are missing, removing their contribution to the magnitude of the field.

Our approach, which only recovers up to degree three, develops an accurate representation of the accelerations, as seen in 4. Higher order terms governing the more complex structure are recovered more accurately than the lower degree coefficients. The contribution of higher degree terms $3 < N < 20$ are approximated in our solution by the lowest order terms, such as J_2, where we see the greatest difference with the VETSA20H solution.

Qualitatively, the magnitude of our recovered accelerations map quite well with the recovered structure in Figure 3. Large geographical formations on the south pole of the asteroid correspond to a very large perturbation to the expected 2-Body accelerations, indicating a key point of interest for geologists. Additionally, the oblateness, or flattening, of the asteroid matches with the larger than expected values for coefficient J_2 computed from the Kaula power law in Eq. 12

Even though our approach does not obtain the high degree coefficients to determine the complexity of the gravitational field, there is no real theoretical limitation with our technique to recover these coefficients. These results show only partial data solutions with a portion of the high altitude orbits, unlike the VESTA20H solution that utilized significantly more data, both optically in addition to ten second at sub-millimeter precision tracking with the DSN. Integrating additional data, especially low altitude orbits, may help determine these high degree coefficients.

5 Conclusion

In this paper we presented a formulation for solving for a set of spherical harmonic coefficients that determine the gravitational field of extraterrestrial bodies without the need for Earth-based tracking systems. We verified this approach through comparison with the state of the art results from the DAWN mission to the asteroid Vesta, and the gravitational results presented in [13]. This approach was able to recover similar results up to degree three utilizing significantly less data.

We believe that our result could be improved up to higher degrees and accuracy simply with the incorporation of the complete high altitude and low altitude orbits. Additionally, the resolution of the 3D reconstruction can be improved significantly by incorporating cycles that have higher overlap between images and with additional coverage of the asteroid's surface.

Future work into utilizing the 3D reconstruction results into the gravitational optimization would provide an interesting extension. Due to the strong relationship between the gravitational perturbations and the geological structure and shape of the target body, incorporation of the curvature, volume, oblateness, and other physical properties as additional constraints could improve the resolution and accuracy of the estimates.

References

[1] S.W. Asmar, A.S. Konopliv, R.S. Park, B.G. Bills, R. Gaskell, C.A. Raymond, C.T. Russell, D.E. Smith, M.J. Toplis, and M.T. Zuber. The gravity field of vesta and implications for interior structure. In *Lunar and Planetary Institute Science Conference Abstracts*, volume 43, page 2600, 2012.

[2] R. Bolles and M. Fischler. A RANSAC-based approach to model fitting and its application to finding cylinders in range data. In *Intl. Joint Conf. on AI (IJCAI)*, pages 637–643, Vancouver, BC, Canada, 1981.

[3] F. Dellaert and M. Kaess. Square Root SAM: Simultaneous localization and mapping via square root information smoothing. *Intl. J. of Robotics Research*, 25(12):1181–1203, Dec 2006.

[4] B.A. Galler and M.J. Fisher. An improved equivalence algorithm. *Communications of the ACM*, 7(5):301–303, 1964.

[5] R. W. Gaskell, O. S. Barnouin-Jha, D. J. Scheeres, a. S. Konopliv, T. Mukai, S. Abe, J. Saito, M. Ishiguro, T. Kubota, T. Hashimoto, J. Kawaguchi, M. Yoshikawa, K. Shirakawa, T. Kominato, N. Hirata, and H. Demura. Characterizing and navigating small bodies with imaging data. *Meteoritics & Planetary Science*, 43(6):1049–1061, June 2008. ISSN 10869379. doi: 10.1111/j.1945-5100.2008.tb00692.x. URL http://doi.wiley.com/10.1111/j.1945-5100.2008.tb00692.x.

[6] R.W. Gaskell and N. Mastrodemos. Lunar Topography from Stereophotoclinometry. *Lunar and Planetary Institute Science Conference Abstracts*, 39:1152, 2008. URL http://adsabs.harvard.edu/abs/2008LPI....39.1152G.

[7] R. I. Hartley and A. Zisserman. *Multiple View Geometry in Computer Vision*. Cambridge University Press, second edition, 2004.

[8] W.M. Kaula. *Theory of satellite geodesy: applications of satellites to geodesy*. Courier Dover Publications, 2000.

[9] K. Konolige. Sparse sparse bundle adjustment. In *British Machine Vision Conf. (BMVC)*, September 2010.

[10] A. S. Konopliv, S. W. Asmar, B. G. Bills, N. Mastrodemos, R. S. Park, C. a. Raymond, D. E. Smith, and M. T. Zuber. The Dawn Gravity Investigation at Vesta and Ceres. *Space Science Reviews*, 163(1-4):461–486, June 2011. ISSN 0038-6308. doi: 10.1007/s11214-011-9794-8. URL http://www.springerlink.com/index/10.1007/s11214-011-9794-8.

[11] A.S. Konopliv, J.K. Miller, W.M. Owen, D.K. Yeomans, J.D. Giorgini, R. Garmier, and J-P. Barriot. A global solution for the gravity field, rotation, landmarks, and ephemeris of eros. *Icarus*, 160(2):289–299, 2002.

[12] A.S. Konopliv, S.W Asmar, W.M. Folkner, Ö. Karatekin, D.C. Nunes, S.E. Smrekar, C.F. Yoder, and M.T. Zuber. Mars high resolution gravity fields from mro, mars seasonal gravity, and other dynamical parameters. *Icarus*, 211(1):401–428, 2011.

[13] A.S. Konopliv, S.W. Asmar, R.S. Park, B.G. Bills, F. Centinello, A.B. Chamberlin, A. Ermakov, R.W. Gaskell, N. Rambaux, C.A. Raymond, et al. The vesta gravity field, spin pole and rotation period, landmark positions, and ephemeris from the dawn tracking and optical data. *Icarus*, 2013.

[14] M.I. A. Lourakis and A.A. Argyros. SBA: A Software Package for Generic Sparse Bundle Adjustment. *ACM Trans. Math. Software*, 36(1):1–30, 2009. doi: http://doi.acm.org/10.1145/1486525.1486527.

[15] D.G. Lowe. Object recognition from local scale-invariant features. In *Intl. Conf. on Computer Vision (ICCV)*, pages 1150–1157, 1999.

[16] N. Mastrodemos, B. Rush, D. Vaughan, and B. Owen. Optical navigation for Dawn at Vesta. *21st AAS/AIAA Space Flight Mechanics Meeting*, (July 2011):1–16, 2011. URL http://trs-new.jpl.nasa.gov/dspace/handle/2014/41960.

[17] J.K. Miller, A.S. Konopliv, P.G. Antreasian, J.J. Bordi, S. Chesley, C.E. Helfrich, W.M. Owen, T.C. Wang, B.G. Williams, D.K. Yeomans, et al. Determination of shape, gravity, and rotational state of asteroid 433 eros. *Icarus*, 155(1):3–17, 2002.

[18] C.A. Raymond, R. Jaumann, A. Nathues, H. Sierks, T. Roatsch, F. Preusker, F. Scholten, R.W. Gaskell, L. Jorda, H-U. Keller, et al. The dawn topography investigation. In *The Dawn Mission to Minor Planets 4 Vesta and 1 Ceres*, pages 487–510. Springer, 2012.

[19] D.A. Vallado. *Fundamentals of astrodynamics and applications*, volume 12. Springer, 2001.